A Kinematic Modeling Study of the Reorganization of Snowfall between Cloud-Top Generating Cells and Low-Level Snowbands in Midlatitude Winter Storms

ANDREW JANISZESKI[a] ROBERT M. RAUBER,[a] BRIAN F. JEWETT,[a] GREG M. MCFARQUHAR,[b,c] TROY J. ZAREMBA,[a] AND JOHN E. YORKS[d]

[a] *Department of Atmospheric Sciences, University of Illinois Urbana–Champaign, Urbana, Illinois*
[b] *Cooperative Institute for Severe and High-Impact Weather Research and Operations, University of Oklahoma, Norman, Oklahoma*
[c] *School of Meteorology, University of Oklahoma, Norman, Oklahoma*
[d] *NASA Goddard Space Flight Center, Greenbelt, Maryland*

ABSTRACT: This paper explores whether particles within uniformly spaced generating cells falling at terminal velocity within observed 2D wind fields and idealized deformation flow beneath cloud top can be reorganized consistent with the presence of single and multibanded structures present on WSR-88D radars. In the first experiment, two-dimensional wind fields, calculated along cross sections normal to the long axis of snowbands observed during three northeast U.S. winter storms, were taken from the initialization of the High-Resolution Rapid Refresh model. This experiment demonstrated that the greater the residence time of the particles in each of the three storms, the greater particle reorganization occurred. For experiments with longer residence times, increases in particle concentrations were nearly or directly collocated with reflectivity bands. For experiments with shorter residence times, particle reorganization still conformed to the band features but with less concentration enhancement. This experiment demonstrates that the combination of long particle residence time and net convergent cross-sectional flow through the cloud depth is sufficient to reorganize particles into locations consistent with precipitation bands. Increased concentrations of ice particles can then contribute, along with any dynamic forcing, to the low-level reflectivity bands seen on WSR-88D radars. In a second experiment, the impact of flow deformation on the reorganization of falling ice particles was investigated using an idealized kinematic model with stretching deformation flow of different depths and magnitudes. These experiments showed that deformation flow provides for little particle reorganization given typical deformation layer depths and magnitudes within the comma head of such storms.

SIGNIFICANCE STATEMENT: Past research with vertically pointing and scanning radars presents two different perspectives regarding snowfall organization in winter storms. Vertically pointing radars often observe cloud-top generating cells with precipitation fallstreaks descending into a broad stratiform echo at lower altitudes. In contrast, scanning radars often observe snowfall organized in quasi-linear bands. This work attempts to provide a connection between these two perspectives by examining how two-dimensional convergent and deformation flow occurring in winter storms can contribute to the reorganization of snowfall between cloud top and the ground.

KEYWORDS: Precipitation; Snowfall; Stratiform clouds; Winter/cool season

1. Introduction

Radar observations of the comma-head region of wintertime extratropical cyclones over the central and eastern United States present two different perspectives on snowfall organization. The first perspective, provided by airborne and ground-based vertically pointing radars, is that precipitation often originates in cloud-top generating cells with precipitation fall streaks emerging from the cells. Cloud-top generating cells, a type of elevated convection, are small regions of locally high reflectivity at cloud top from which a reflectivity trail characteristic of falling snow particles originates (American Meteorological Society 2023). They are ubiquitous at cloud top, 1–2 km deep, 0.5–2 km wide, and typically with updrafts

of 1–2 m s^{-1} (McFarquhar et al. 2011; Rosenow et al. 2014; Kumjian et al. 2014). The reflectivity fallstreaks appearing on radar are often sheared, and typically descend and merge into a more stratiform radar echo lower in the clouds. Studies describing cloud-top generating cells and precipitation fall streaks have appeared in the literature over seven decades (Marshall 1953; Gunn et al. 1954; Wexler 1955; Douglas et al. 1957; Wexler and Atlas 1959; Carbone and Bohne 1975; Hobbs and Locatelli 1978; Syrett et al. 1995; Stark et al. 2013; McFarquhar et al. 2011; Kumjian et al. 2014; Rosenow et al. 2014; Rauber et al. 2014b, 2017; Plummer et al. 2014, 2015). Idealized modeling studies show that cloud-top generating cells can result from cloud-top radiative cooling, be enhanced or suppressed by the cloud-top stability profile, and organize differently based on the vertical wind shear across the cloud-top region (Keeler et al. 2016a,b, 2017). Many studies (e.g., Houze et al. 1981; Rutledge and Hobbs 1983; Browning 1983; Sienkiewicz et al. 1989; Syrett et al. 1995; Schultz et al. 2004; Stark et al. 2013; Cunningham and Yuter 2014) have described generating cells as one component of a "seeder–feeder" mechanism (Bergeron 1950), the

generating cells "seeding" ice particles into the stratiform "feeder" layer below, with large-scale convergence providing the moisture source for growth of particles below the generating cell level (Matejka et al. 1980; Herzegh and Hobbs 1980; Rutledge and Hobbs 1983; Browning 1983).

The second perspective, provided by weather surveillance radars, is that zones of heavier snowfall are often organized in quasi-linear banded structures characterized by enhanced regions of radar reflectivity factor (hereafter, reflectivity) with quasi-linear shapes (i.e., long axis:short axis ratio $\geq$ 2:1). Bands are normally embedded within broader regions of lower reflectivity associated with lighter snowfall. Numerous studies have shown that near-surface banding typically occurs in the vicinity of midtropospheric frontal boundaries (e.g., Nicosia and Grumm 1999; Novak et al. 2004, 2009, 2010; Stark et al. 2013; Kumjian and Lombardo 2017). The near-surface primary band is frequently coincident with an axis of low and midlevel frontogenesis (Nicosia and Grumm 1999; Novak et al. 2004, 2009, 2010; Stark et al. 2013; Kumjian and Lombardo 2017). Many cyclones exhibit several bands simultaneously. Multibanded precipitation has been hypothesized to be related to phenomena such as gravity waves (Sanders and Bosart 1985; Yang et al. 2001), frontal irregularities (Hobbs and Locatelli 1978), elevated convection (Rauber et al. 2014a; Rosenow et al. 2014), and other sources, but the exact causes of multibanded precipitation remain poorly understood (Schultz and Knox 2007; Ganetis et al. 2018). Snowfall rates within bands can often exceed 2.5 cm h^{-1} (1 in. h^{-1}). Novak et al. (2004) and Ganetis et al. (2018) document various types of banding structures, with different storms exhibiting a single band, single large bands co-occurring with sets of smaller bands, multibands only, and nonbanded storms. Banded features can exhibit different horizontal lengths and widths.

Explanations for the presence of a single dominant precipitation band center on the role of frontogenesis resulting from horizontal deformation flow acting upon a preexisting temperature gradient (Bergeron 1928; Petterssen 1936; Sanders 1955; Stone 1966). The relationship between precipitation bands, the vertical circulation associated with frontogenetical forcing, and the release of conditional and/or conditional symmetric instability has been explored in numerous studies (e.g., Schultz and Schumacher 1999; Novak et al. 2009; Lackmann and Thompson 2019). Thorpe and Emanuel (1985), Emanuel (1985), Sanders and Bosart (1985), and Sanders (1986) showed that frontogenetic forcing in the presence of weak positive symmetric stability will increase the intensity of precipitation within the primary band while decreasing the width of the associated updraft. Novak et al. (2008) used high-resolution modeling to link mesoscale band formation with changes in forcing, stability, and moisture. They found that band formation occurred as frontogenetic forcing and conditional stability increased. Novak et al. (2010) further examined the roles of frontogenesis, conditional symmetric instability, conditional instability, and inertial instability in the context of band formation through reanalysis and radar data, finding that in the regions of frontogenetic forcing, stability could be either weakly stable or conditionally unstable.

In general, the primary precipitation band appearing on surveillance radars as the result of frontogenesis must result from any or all of three processes: 1) concentration of ice particles into an elongated narrow region as a result of convergent and/or deformation flow, 2) growth of particles within an elongated updraft as a result of the secondary circulation associated with frontogenesis, and 3) growth of particles within convection triggered within the updraft associated with the secondary circulation. This paper focuses exclusively on the first process, with the goal of providing insight on how cloud-top generating cells and near-surface banded features are related. Specifically, we examine the reorganization of ice particles falling beneath cloud-top generating cells subject to two-dimensional convergence and stretching deformation kinematic flow fields in an attempt to bridge the two perspectives.

We conducted two separate experiments to explore how flow kinematics can reorganize snowfall beneath cloud-top generating cells. In the first experiment we explore whether convergence of particles originating near cloud top in uniformly spaced generating cells, falling at Doppler-radar-observed fall velocities within observed 2D wind fields in the stratiform region of winter storms, can be reorganized consistent with the presence of single and multibanded structures observed with surveillance radars. The wind fields are from the initialization of the High-Resolution Rapid Refresh (HRRR) model, and the radar data from three northeast U.S. winter storms. In the second experiment, we examine the potential role of flow deformation in the reorganization of ice particles using an idealized kinematic model with particle fall velocities and stretching deformation flow having values and depths characteristic of winter cyclones.

Section 2 describes generalized profiles of near-vertical radial Doppler velocities in winter storms. Section 3 presents the idealized model framework used to analyze the impact of two-dimensional convergence and the results of that analysis. Section 4 examines the potential reorganization of ice particles falling beneath cloud-top generating cells subject to stretching deformation flow fields. Section 5 provides the conclusions of the study.

2. Characteristics of the stratiform region of winter cyclones observed during IMPACTS and PLOWS

In a stratiform cloud with minimal updraft velocities, the residence time (t_r) of a particle falling from cloud top to the ground is controlled by the particle fall depth and the particle fall velocity profile (V_f). Representative values of particle fall depth and terminal velocity were identified using recent field campaign observations of winter snowstorms. One such field campaign is the Investigation of Microphysics and Precipitation in Atlantic Coast Threatening Snowstorms (IMPACTS). IMPACTS consisted of three 6-week field deployments (2020, 2022, 2023) utilizing a complementary suite of remote sensors on the National Aeronautics and Space Administration (NASA) Earth Resources 2 (ER-2) high-altitude aircraft and in situ instruments on the NASA P-3 aircraft (McMurdie et al. 2019, 2022). The Cloud Physics Lidar (CPL) is a multiwavelength (355, 532, 1064 nm) elastic backscatter lidar that flies on the ER-2 as part of the IMPACTS project (McGill et al. 2002). The CPL provides cloud-top heights through measurements of the 532 nm total attenuated backscatter at 30 m vertical resolution (Yorks et al. 2011). Figure 1 shows that cloud-top heights measured during the
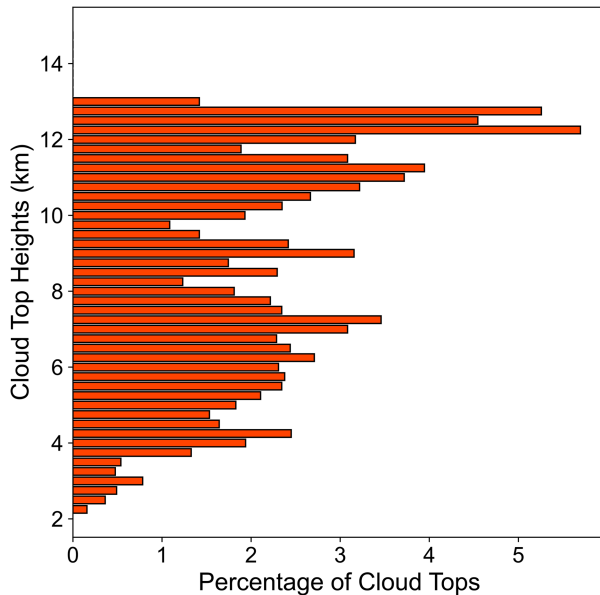
FIG. 1. Percentage of CPL-determined cloud tops at a given altitude from all sampled storms during 2020 and 2022 IMPACTS deployments in winter storms.

IMPACTS 2020 and 2022 deployments were primarily between 6 and 12 km. The Cloud Radar System (CRS) is a nadir pointing W-band (94 GHz) radar flown on the ER-2 during IMPACTS that provides reflectivity and vertical radial velocities (V_r; Walker Mclinden et al. 2021). The median V_r below cloud top from CRS during IMPACTS 2020 and 2022 in the snowfall regions of the sampled winter cyclones was approximately −0.8 m s^{-1}, decreasing to near −1.2 m s^{-1} at the surface, as shown by Varcie et al. (2023, Fig. 2, their Fig. 8c). This range of velocities is representative of terminal velocities of unrimed ice particles in winter storms (Heymsfield 1972; Mitchell 1996). These values are also consistent with similar measurements made in stratiform winter clouds with the University of Wyoming King Air W-band Cloud Radar (EOL/PLOWs 2023; Rosenow et al. 2014, Fig. 3, their Fig. 10). For this study experiments were conducted where the particle release altitude (z_i) ranged from 6 to 10 km with several V_f profiles, V_f decreasing from −0.8 to −1.2 m s^{-1} between the release altitude and 1 km and a constant V_f of −0.8, −1.0, and −1.2 m s^{-1}.

3. Reorganization of particles by two-dimensional convergence

This section explores whether convergence of particles falling beneath cloud top from uniformly spaced generating cells falling at velocities consistent with Doppler radar measurements within observed 2D wind fields can be reorganized consistent with the presence of single and multibanded structures present on WSR-88D radars.

a. Three banded northeast U.S. snowstorms

Three storms exhibiting different banding structures were selected for this analysis. The first storm on 16–17 December
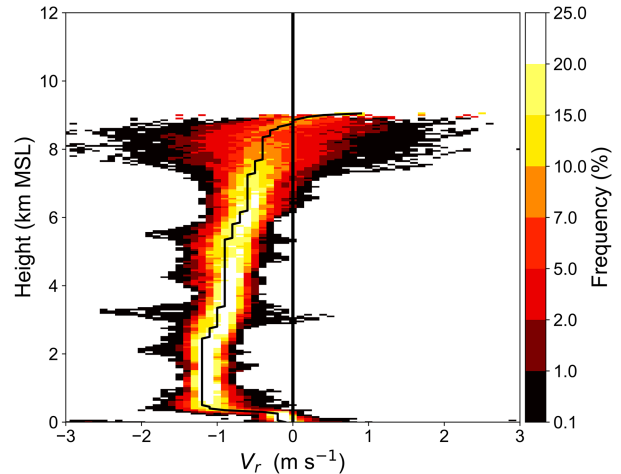

FIG. 2. Contour frequency by altitude diagram (CFAD) of vertical radial velocities measured by the CRS on the NASA ER-2 aircraft in the stratiform region of the comma head of a winter storm on 7 Feb 2020. The black contour shows the median radial velocity values (from Varcie et al. 2023, their Fig. 8c).

2020 had a single precipitation band anchored over the Binghamton, New York, area that produced heavy snowfall. The second storm on 29–30 January 2022 had three precipitation bands within the comma head of a rapidly deepening northeast U.S. snowstorm. The third storm on 4 February 2022 produced weak linear bands along a frontal boundary. These storms represent a range of scenarios found in northeast U.S. snowstorms.
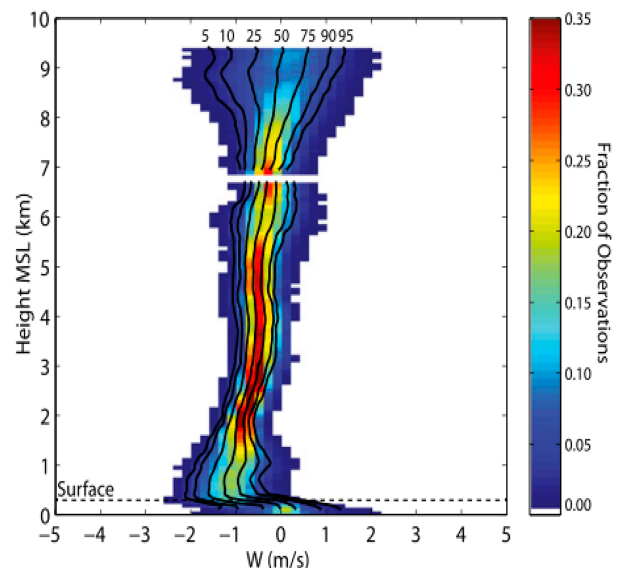

FIG. 3. CFAD of vertical radial velocities measured by the W-band University of Wyoming Cloud Radar on the National Center for Atmospheric Research C-130 aircraft in the stratiform region of the comma head of a winter storm on 8–9 Dec 2009. The black contours show the percentage of observations with vertical radial velocities greater than the number noted on the contour. The median V_r contour most closely represents V_f of particles (from Rosenow et al. 2014, their Fig. 10).
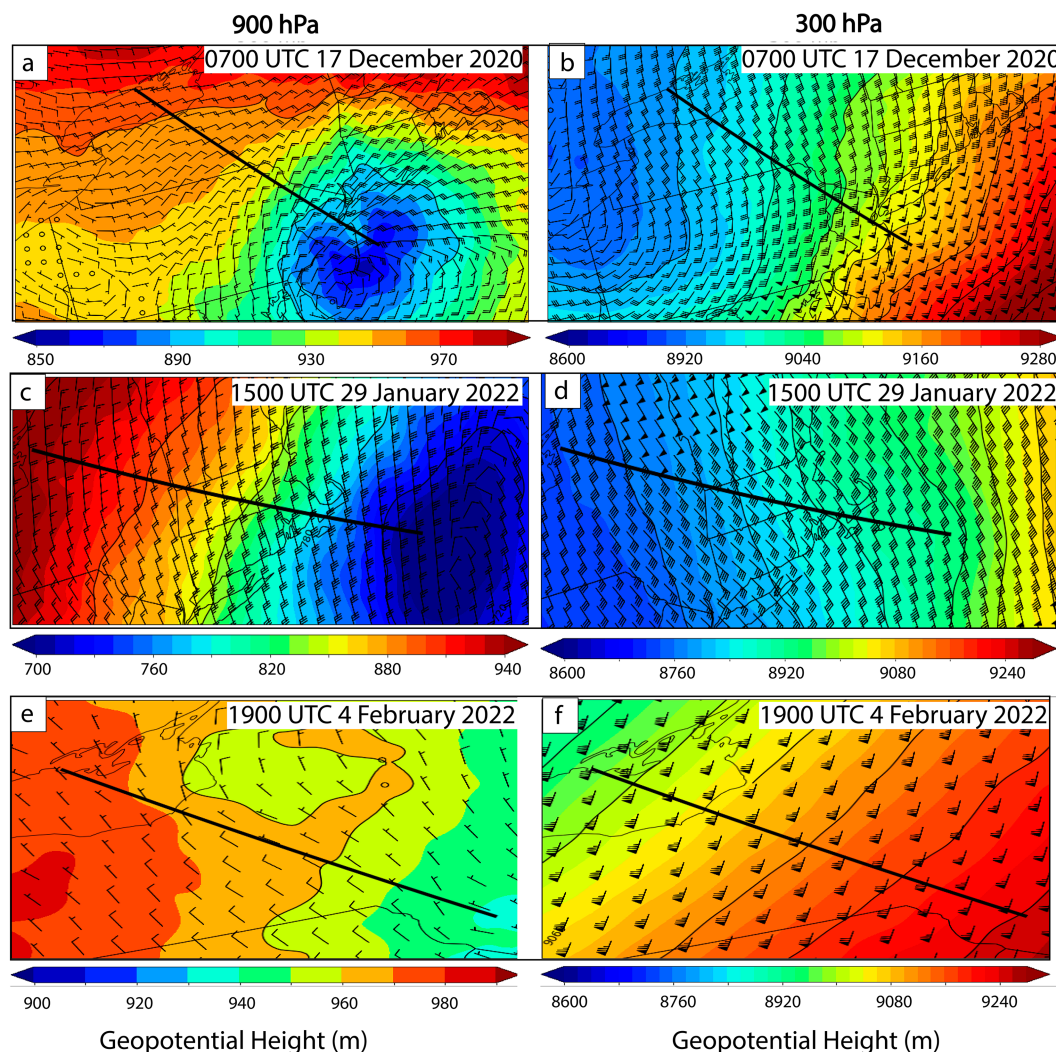
FIG. 4. The 900 hPa winds (m s^{-1}) and geopotential height (m) from the HRRR model initialization at (a) 0700 UTC 17 Dec 2020, (c) 1500 UTC 29 Jan 2022, and (e) 1900 UTC 4 Feb 2022. The 300 hPa winds (m s^{-1}) and geopotential height (m) at (b) 0700 UTC 17 Dec 2020, (d) 1500 UTC 29 Jan 2022, and (f) 1900 UTC 4 Feb 2022.

1) 16–17 DECEMBER 2020 STORM

A significant snowfall event associated with a major northeast U.S. snowstorm impacted the interior of the mid-Atlantic and New England states on 16–17 December 2020. At 0700 UTC 17 December 2020, a low geopotential height center at 900 hPa, based on the initialization of the 0700 UTC 3-km-resolution HRRR model, was located over southern New Jersey (Fig. 4a). WSR-88D reflectivity measurements from Binghamton (KBGM), Montague, New York (KTYX), and Albany, New York (KENX), at 0700 UTC 17 December 2020 show a clear single band feature approximately 110 km wide with enhanced reflectivity of over 27 dBZ centered near Binghamton (Fig. 5a). This band produced upward of 100 cm (40 in.) of snow in the Binghamton area over a 12 h period (NWS Binghamton). Using the initialization of the 0700 UTC 3-km-resolution HRRR model, the along cross-section component of the wind (v, positive toward the northwest) was calculated along a cross section normal to

the long axis of the band between 1 and 10 km altitude (Fig. 5b). The distance D from the northwest corner of the cross section is used to reference the horizontal position of features described below. High values of v greater than 40 m s^{-1} from the southeast in the upper-right region of Fig. 5b are the consequence of a south to southeasterly jet flowing with a significant component along the cross section from southeast to northwest (Fig. 4b). At 900 hPa, diffluent flow was present in the vicinity of the cross section with winds having a ~5 m s^{-1} v component toward the northwest on the west side of the cross section and a component increasing from −5 to −20 m s^{-1} toward the southeast on the east side (Fig. 5b, see arrows). A sharp vertical gradient of v was present between 1 and 3 km altitude with 15 m s^{-1} km^{-1} shear found across much of the right half of the cross section. Two-dimensional convergence is overlaid on the cross-sectional flow in Fig. 5b. A region of stronger convergence extended from an altitude of 10 to 4 km slantwise downward from $D = 300$ to 500 km.
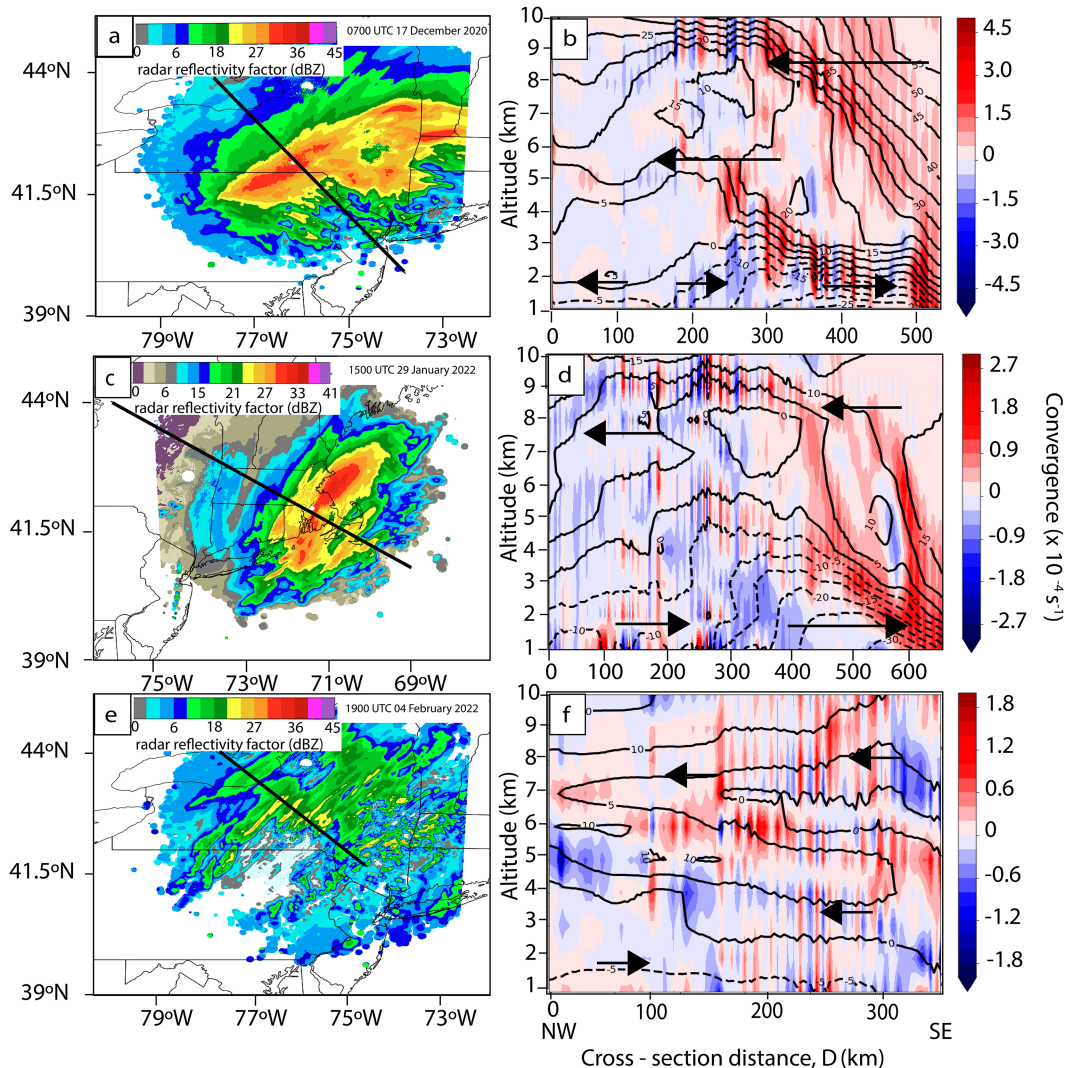
FIG. 5. WSR-88D radar reflectivity (dB*Z*) from (a) KBGM, KTYX, and KENX at 0700 UTC 17 Dec 2020, (c) KENX and KBOX at 1500 UTC 29 Jan 2022, and (e) KBGM, KTYX, and KENX at 1900 UTC 4 Feb 2022. Along cross-sectional wind component v (m s^{-1}; contours every 5 m s^{-1}) and two-dimensional convergence (shading; 10^{-4} s^{-1}), for (b) 0700 UTC 17 Dec 2020, (d) 1500 UTC 29 Jan 2022, and (f) 1900 UTC 4 Feb 2022. The arrows in (b), (d), and (f) represent wind direction.

Additionally, there were convergence zones within the region of strong vertical wind shear from D = 250 to 500 km between 1 and 4 km altitude. Below 1 km altitude, the cross-sectional flow encountered hills and mountains which interfere with the flow. This region was omitted from the analyses in section 4.

2) 29–30 JANUARY 2022 STORM

A major northeast U.S. snowstorm impacted southeastern New England and the eastern mid-Atlantic from 29 to 30 January 2022. Blizzard conditions were reported at major East Coast cities such as Boston, Massachusetts. Several snowbands were observed on the WSR-88D surveillance radars along the East Coast. Figure 5c shows reflectivity at 1500 UTC from the KENX

and Boston (KBOX) WSR-88D radars on 29 January 2022 showing a wide band with maximum reflectivity of 30 dB*Z* and two narrower bands flanking the major band. The higher reflectivity region of the primary band ranged between 30 and 60 km wide over SE Massachusetts, Rhode Island, and eastern Connecticut. A strong northwesterly flow of 30–35 m s^{-1} was present along the coastal region at 900 hPa, with winds decreasing in magnitude to 15–20 m s^{-1} to the west (Fig. 4c). These strong winds lead to a maximum of $v > -20$ m s^{-1} toward the southeast end of the cross section for D = 330–600 km below 2–2.5 km altitude (Fig. 5d). A southeasterly jet was present aloft (Fig. 4d). The upper-level v wind component above 4 km was relatively weak (<15 m s^{-1}) except near 10 km altitude where $v > 15$ m s^{-1}. Two-dimensional convergence overlaid on v in Fig. 5d shows a region of convergent flow

sloping upward between 1 and 9 km altitude for $D > 400$ km. Divergent flow occurred across the west half of the cross section, particularly between $D = 300$ and 400 km below 4 km altitude.

3) 4 February 2022 storm

A frontal system exhibiting multibanded structure with weaker reflectivity impacted the northeast United States on 4 February 2022. Narrow bands occurred along a long frontal boundary that stretched from Texas to Maine with several embedded shortwaves traversing the front. WSR-88D radars KENX, KBGM, and KTYX showed snowfall occurring over much of upstate New York at 1900 UTC with the snowfall arranged in a series of bands that were 10–20 km wide and had maximum reflectivity of 21–24 dBZ (Fig. 5e). A weak flow of $\sim$5 m s^{-1} from the northwest was present at 900 hPa across the region (Fig. 4e). These weak winds were near parallel to the cross section, resulting in a $\sim$−5 m s^{-1} v component in the lower levels in Fig. 5f. A strong 300 hPa jet flowed almost normal to the cross section (Fig. 4f) resulting in a 5–10 m s^{-1} v component in the upper levels of the cross section (Fig. 5f). Two-dimensional convergence overlaid on v in Fig. 5f shows numerous convergence/divergence couplets associated with very weak variations in the v component. Overall general weak convergent flow was present between 5 and 6.5 km altitude for $D > 100$ km and between 7 and 10 km for $D = 250$–300 km. Weak divergent flow was present for $D < 250$ km between 3 and 5 km altitude (Fig. 5f).

b. Kinematic framework

The kinematic framework uses the parallel wind component along each cross section calculated from the HRRR model wind field initialization for each event. For all experiments, particles were arranged in a line across the entirety of D, spaced 10 m apart at either one or three initial particle altitudes, $z_i = 6$, 8, and/or 10 km. The initial spacing of particles at 10 m results in an initial distribution of 1000 particles per 10-km-wide bin. In experiments where particles were released from three altitudes simultaneously, a total of 3000 particles were present in each bin, 1000 at each altitude.

The trajectory of a falling particle depends upon the particle's terminal velocity, any vertical circulations within the storm, and the horizontal wind field. The clouds were assumed to be stratiform so that particles fell at the velocity represented by the median value of the radial velocities from the Doppler measurements. Ice particle terminal velocity in general depends upon the growth mechanisms that the particle undergoes as it falls from its point of formation to the ground, and the change in air density with altitude (Pruppacher and Klett 1997, 438–439). In stratiform regions where supercooled liquid water is less likely to be present (Varcie et al. 2023) ice particles falling from cloud-top generating cells grow first by diffusion, and later by aggregation (Kumjian et al. 2014). The impact of these growth mechanisms on the particle fall velocity is evident in the contoured frequency by altitude diagrams (CFADs) in Figs. 2 and 3 where the median radial velocity (an approximate estimate of particle terminal velocity) decreases from $\sim$−0.8 m s^{-1} high in the cloud to $\sim$−1.2 m s^{-1}

near the surface. These values are consistent with many measurements of terminal velocities of unrimed particles (see summary in Rosenow et al. 2014, their Fig. 2).

In this paper we do not attempt to simulate the full range of possible microphysical processes as particles fall from cloud top to the ground, but rather parameterize their fall velocity based on the range of median radial velocities evident on CFADs collected in the stratiform region of winter storms (e.g., Figs. 2 and 3). Specifically, we allow the particles to fall from altitudes of 6, 8, and 10 km with fall velocities ranging from −0.8 m s^{-1} at the starting altitude to −1.2 m s^{-1} at 1 km altitude. In these experiments we assume that no melting occurs in the lower levels so the particles reach the ground as snow. For completeness, we also conduct simulations using constant fall velocities typical of unrimed ice particles in winter storms (Heymsfield 1972; Mitchell 1996). The fall velocities in these experiments were $V_f = -0.8$, −1.0, or −1.2 m s^{-1}. The z_i values and range of V_f provide for a total residence time, $t_r = (z_i - 1)/V_f$, of ice particles between 1.2 and 3.1 h (4167 and 11 250 s) during their fall between cloud top and the 1 km level, where they are assumed to be observable on the lowest scan of a WSR-88D radar.

Particle horizontal and vertical motion was calculated using a two-step bilinear interpolation scheme, similar to that of Draxler and Hess (1998). Each second, the scheme calculated, in the first step, an estimated particle final position (x_e, y_e) using the wind components at the particle initial position (x_i, y_i). In the next step, the wind components at the midpoint between (x_i, y_i) and (x_e, y_e) were determined and used to calculate the actual particle final position (x_f, y_f). Particles then fell at the assigned V_f and were transported by the horizontal wind for one second. The process was then repeated until the particles reached 1 km altitude.

c. Results

1) 16–17 December 2020 storm

Critical to this research is to determine if the horizontal flow alone can reorganize ice particles beneath cloud top such that increased particle concentrations are found collocated with, or near high reflectivity quasi-linear bands. The experiment with fall velocities becoming more negative with decreasing altitude from $z_i = 10$ km will be used as the control experiment for the case studies. Figure 6 shows the results of the control experiment, a histogram of particle concentration in 10 km wide bins at 1 km altitude overlaid on top of the KBGM WSR-88D reflectivity at 0700 UTC 17 December 2020, when heavy snow was falling over Binghamton. The residence time of the particles was 8219 s or 2.3 h. The maximum reflectivity in the band was located at $D = 233$ km from the left end of the cross section. In Fig. 6a, local maxima with two distinct peaks in particle concentration is shown with one collocated with the observed reflectivity maximum at $D = 230$ km and the other, the largest peak, found at $D = 320$ km. To the northwest of the band, a more uniform region of concentration values, between 500 and 800 particles per bin, were located within a region of lower reflectivity values ranging between 8 and 18 dBZ. Meanwhile to the southeast of the main band, the concentration reduced to zero. The reflectivity in that area was low
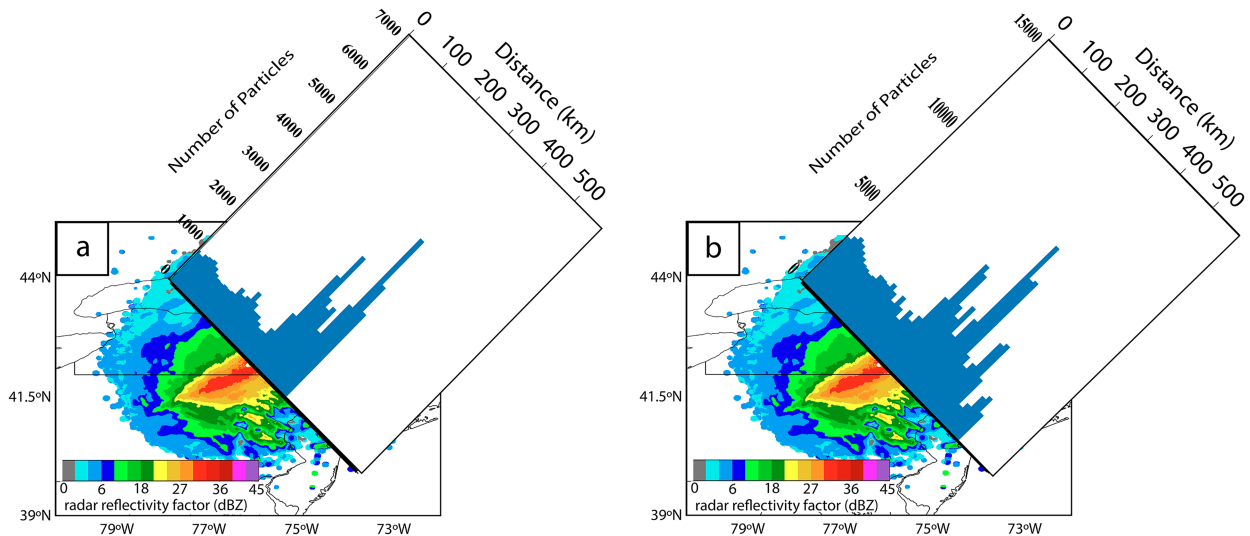
FIG. 6. (a) Overlay of 1-km-altitude particle concentration on top of radar reflectivity from KBGM, KTYX, and KENX at 0700 UTC 17 Dec 2020 for (a) particles released at 10 km and (b) particles released at 10, 8, and 6 km simultaneously.

($\sim$2–12 dBZ). Figure 6b shows the experiment where particles were released from 6, 8, and 10 km simultaneously. Maxima in particle concentration are still located in the vicinity of the higher reflectivity, with the maximum concentration again at $D = 320$ km, although the maxima are smaller relative to the rest of the distribution. The distribution extends farther to the southeast consistent with the reflectivity. Figures 7a–c compare particle concentration distributions for experiments with particle release altitudes of 10, 8, and 6 km, respectively, all with decreasing fall velocities with decreasing altitude. The residence times of particles in the flow for these experiments were 8219, 7258, and 5225 s, respectively. With decreased residence time, less particle reorganization occurred such that distinct maxima became less apparent.

Figures 8a–i show particle concentration distributions from all experiments using a single particle release altitude and constant particle fall velocity. Figures 8a–c show experiments with $z_i = 10$ km, resulting in a 9 km particle fall distance and longer residence times; V_f in these experiments were -1.2 m s^{-1} in Fig. 8a, -1.0 in Fig. 8b, and -0.8 m s^{-1} in Fig. 8c. This resulted in residence times of $t_r = 7500$, 9000, and 11 250 s increasing from Fig. 8a to Fig. 8c. Figures 8d–f have the same V_f, but with $z_i = 8$ km, resulting in a 7 km particle fall distance and $t_r = 5833$, 7000, and 8750 s, respectively. Figures 8g–i also have the same V_f sequence but with $z_i = 6$ km, resulting in a 5 km particle fall distance, and $t_r = 4167$, 5000, and 6250 s, respectively. The concentration in Figs. 8a–c show a broad increase in particle concentrations extending from $D = 220$ to 330 km with two local maxima, one centered between $D = 300$ and 330 km, and a second of smaller magnitude near $D = 250$ km. The values of the peak concentration increased as residence time increased. For example, at $t_r = 7500$ s, the maximum concentration was
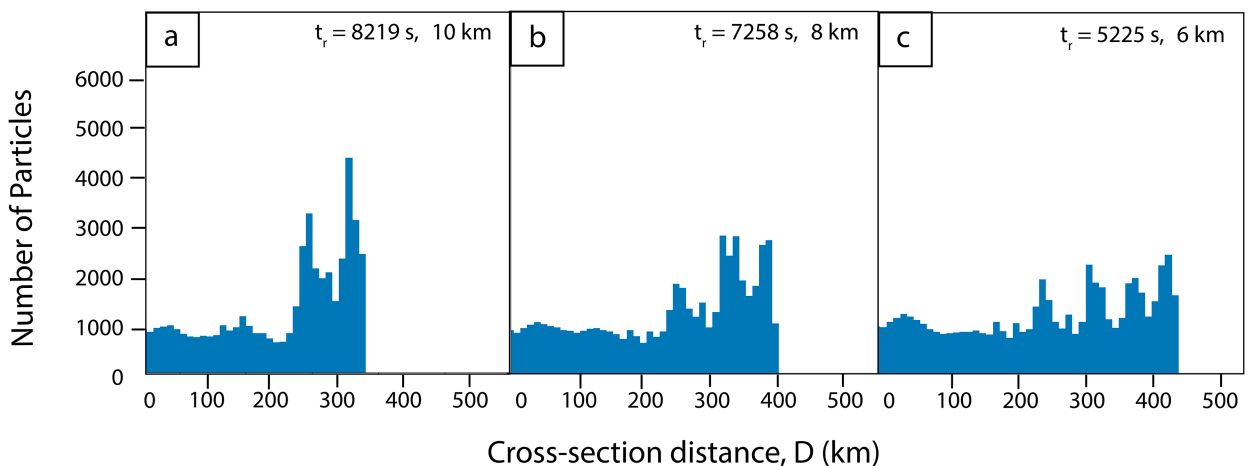

FIG. 7. Particle concentration distribution at 1 km altitude in the 16–17 Dec 2020 storm for particles released at (a) 10, (b) 8, and (c) 6 km with increasing fall velocity with decreasing altitude.
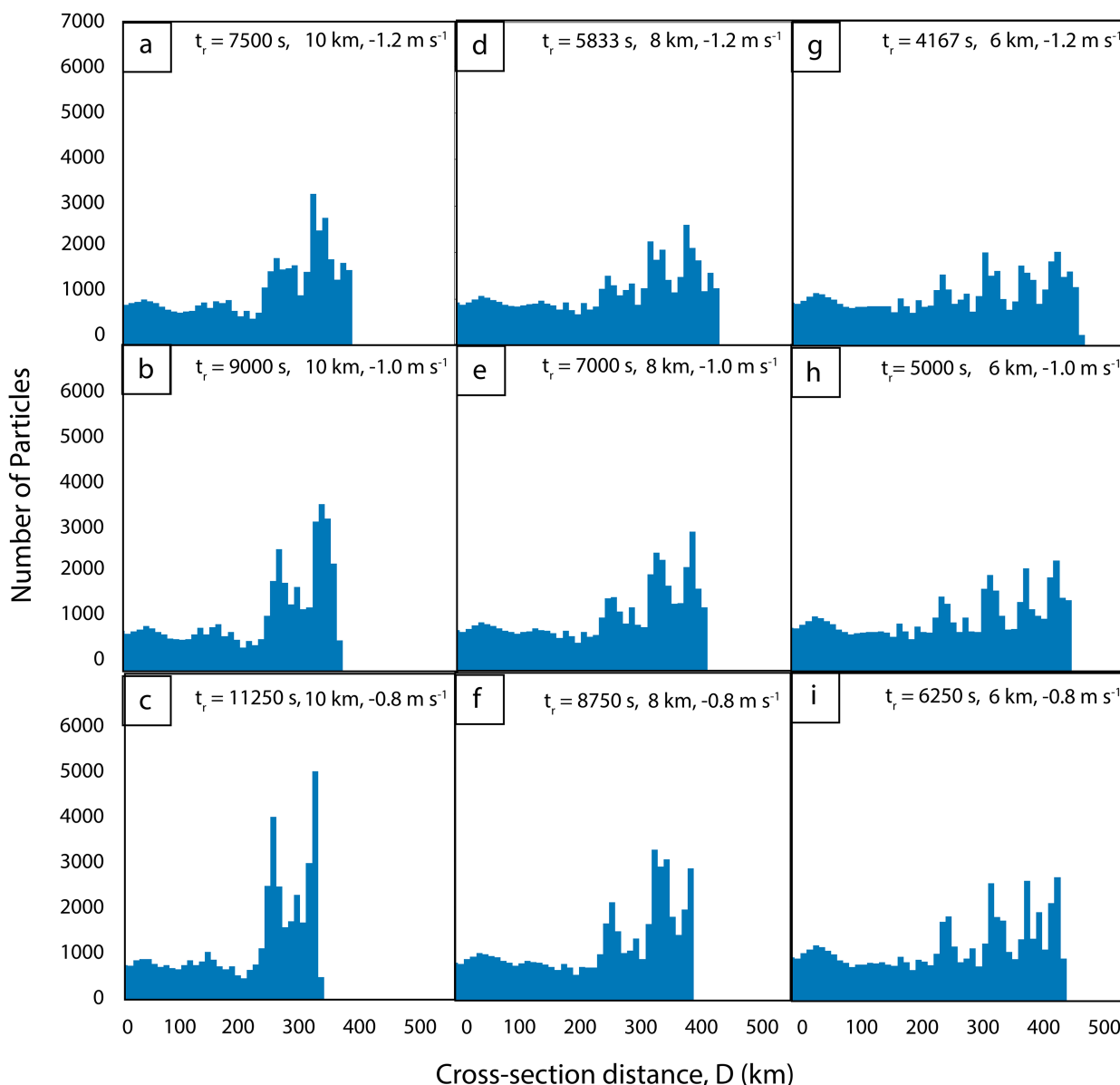
FIG. 8. Particle concentration distribution at 1 km altitude for all values of t_r, z_i, and V_f for 16–17 Dec 2020.

3228 particles per bin (Fig. 8a), whereas for $t_r = 11\,250$ s, the concentration was 4761 particles per bin (Fig. 8c). In Figs. 8g–i, the particle concentration distributions shifted farther southeastward and with smaller residence times, and exhibited either three or four smaller local maxima compared to Figs. 8a–c.

Overall, these experiments together highlight the importance of both residence time and the along cross-section flow in particle reorganization. For experiments with $z_i = 10$ km, particles were subject to a strong southeasterly flow that decreased in magnitude, for example, 50 to 10 m s^{-1} at 8 km from southeast to northwest along the cross section (Fig. 5b). This resulted in an accumulation of particles as they fell to 6 km altitude through a region of convergence of 1.5×10^{-4} to 4×10^{-4} s^{-1} between 6 and 10 km altitude for $D = 300$–450 km

(see Fig. 5b). Next, particles were subject to narrow horizontal regions of convergent flow of 2.5×10^{-4} to 3×10^{-4} s^{-1} near $D = 250$ and 300 km, respectively. This occurred in a layer of 10 m s^{-1} km^{-1} vertical wind shear between 2 and 5 km altitude for $225 < D < 280$ km, and 15 m s^{-1} km^{-1} between 1 and 3 km altitude for $D > 300$ km (see Fig. 5b). Below 2–2.5 km altitude, the flow was northwesterly. Under these conditions, the combination of greater residence time and movement through two convergent flow regions resulted in the particle concentration maximum seen in Figs. 8a–c for $D = 300$–330 km and $D = \sim250$ km. In Figs. 8d–f with lower initial z_i and smaller residence times, the particle concentration distributions all had smaller concentration maxima, a result of less or no time exposed to the aforementioned convergent flow region at or above 6 km
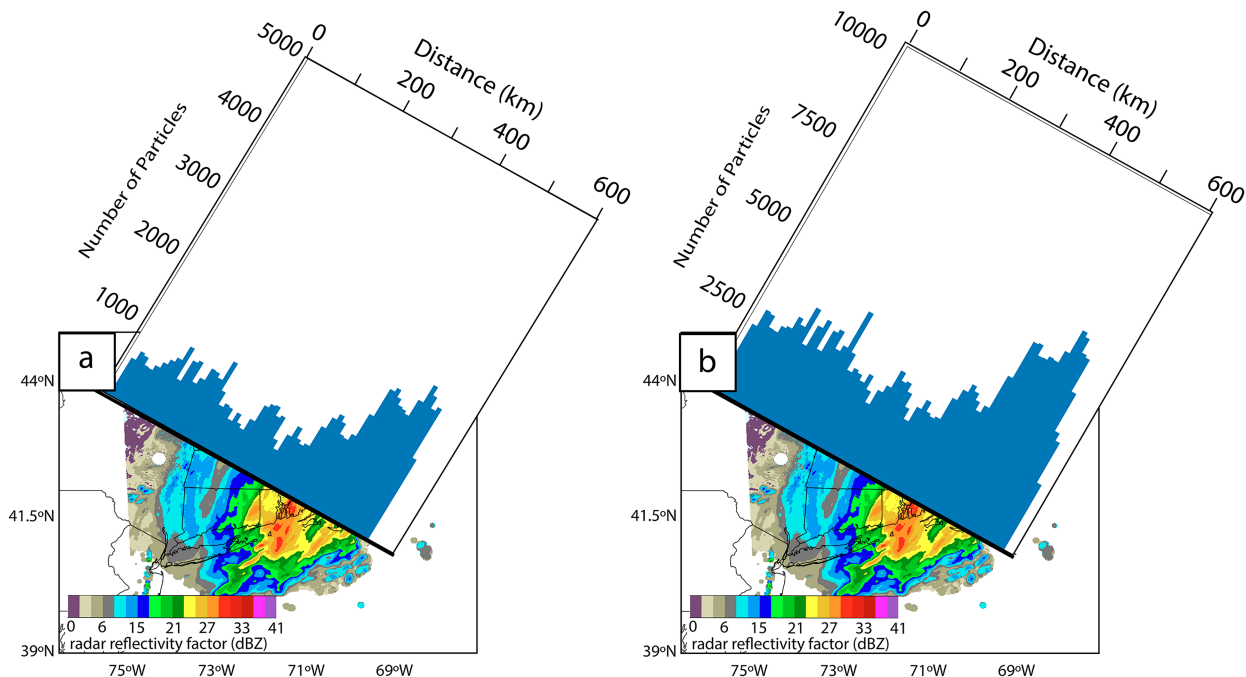
FIG. 9. As in Fig. 6, but for 1500 UTC 29 Jan 2022. (a) Overlay of 1-km-altitude particle concentration on top of radar reflectivity from KBOX and KENX at 1500 UTC 29 Jan 2022 for (a) particles released at 10 km and (b) particles released at 10, 8, and 6 km simultaneously.

altitude. In Figs. 8g–i, several local maxima were found near D = 250, 300–320, 380, and 410 km directly corresponding to several convergence maxima between either 4–6 or 2–4 km altitude. Furthermore, the distributions extended farther to the southeast with decreased residence times because particles were not transported as far to the northwest after release and were displaced farther southeast beneath 2 km altitude in the northwesterly flow.

2) 29–30 JANUARY 2022 STORM

Figure 9a, the control experiment at 1500 UTC 29 January 2022, shows the resulting particle concentration distribution at 1 km altitude overlaid on the WSR-88D reflectivity. At the southeastern side of the cross section, a maximum of 2141

particles per bin appears within 50 km of the two most eastern bands. A lesser peak of particle concentration of 1881 particles per bin directly aligns with the westernmost band. The greatest WSR-88D reflectivity values were near, but not exactly, collocated with the highest concentration values. Farther northwest, numerous local particle concentration maxima and minima extended all the way to the northwest terminus of the cross section at D = 0 near Watertown, New York. The reflectivity shows some weak multibanded structure there, but the locations of the weak reflectivity maxima do not correspond directly with local concentration maxima. Figure 9b shows the experiment where particles were released from all three altitudes simultaneously. As with the control experiment,
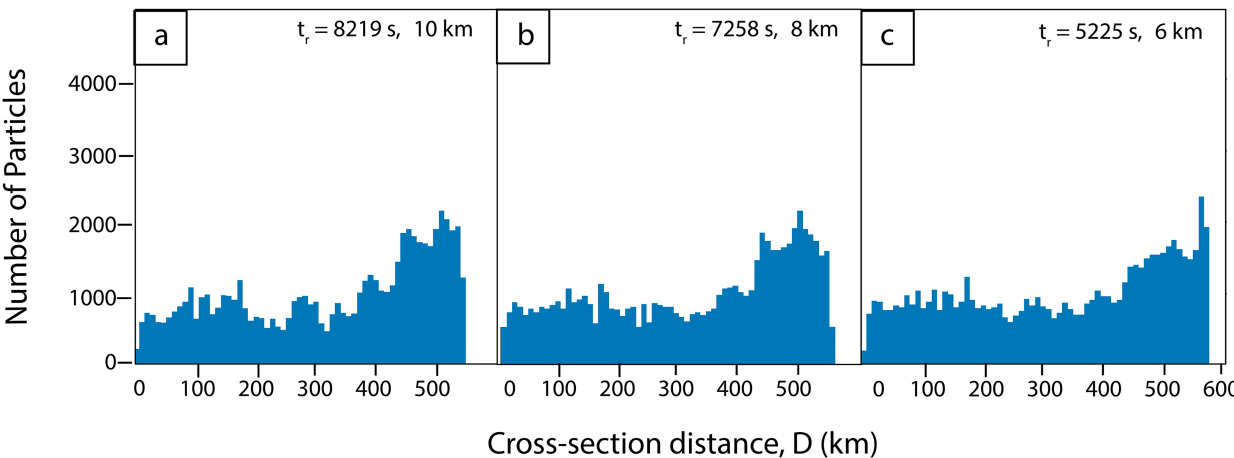

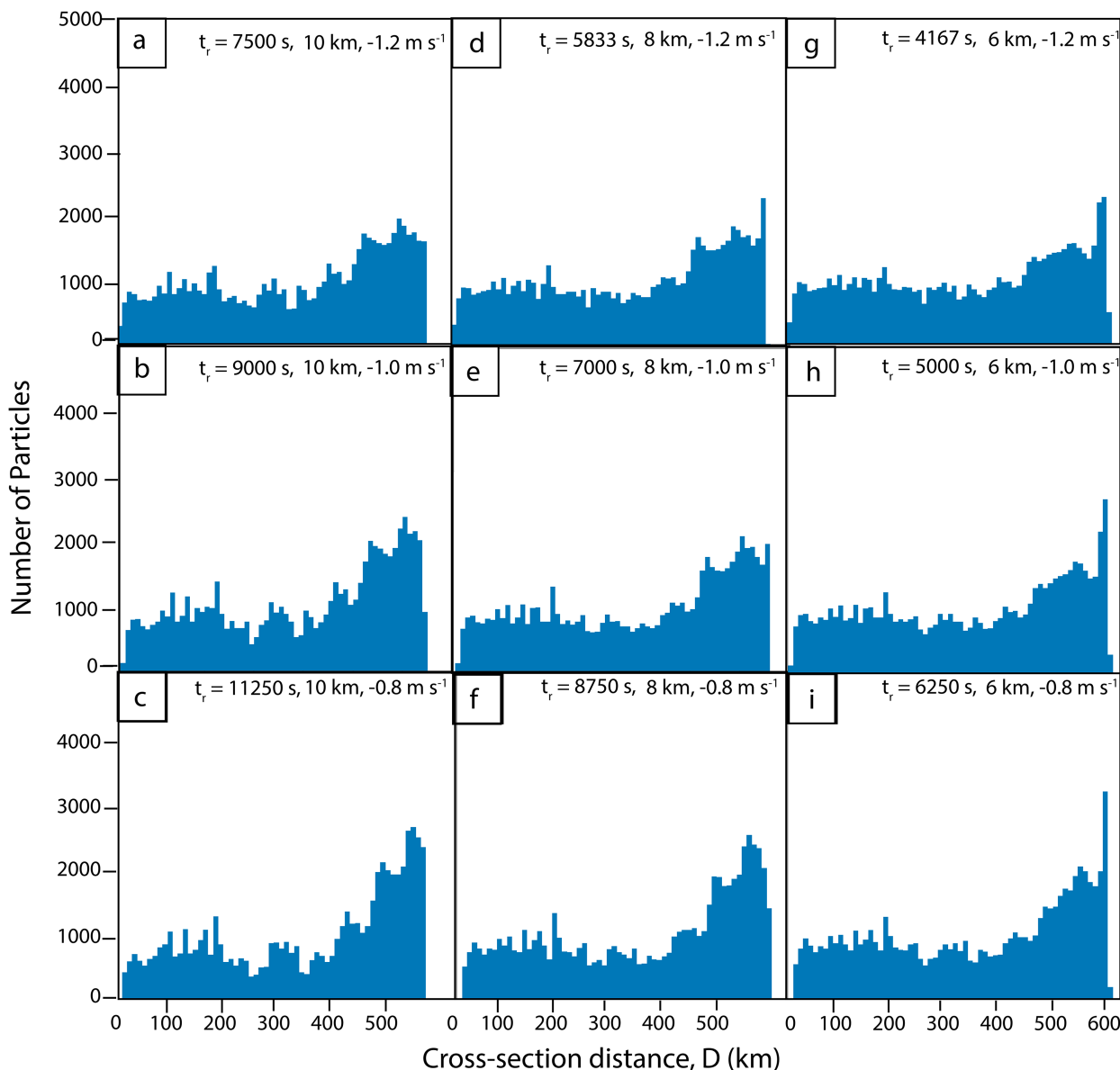FIG. 10. As in Fig. 7, but for 29–30 Jan 2022.

FIG. 11. As in Fig. 8, but for 1500 UTC Jan 2022.

an approximate doubling of the original particle concentrations occurred in the region of the major band. Figures 10a–c compare results for particle releases at z_i = 10, 8, and 6 km. In this storm, the reduction in residence time only had a minor effect on particle reorganization with the smallest residence time having a slightly diminished peak concentration.

Figures 11a–i show particle concentration distributions for all experiments with the constant V_f, for the same z_i and t_r as Figs. 8a–i. The particle concentration distributions were similar for all experiments with a broad region of increased concentrations for $D > 450$ km. A maximum particle concentration of 3187 particles per bin was found at $D = 600$ km in Fig. 11i. Again, the experiment with the maximum residence time in Fig. 11c had the largest concentration maximum, aside

from a sharp particle maximum in one bin (Fig. 11i). The broad region of increased particle concentration is a consequence of the zones of convergent flow extending upward from 1 to 8 km between $D = 600$ and 400 km (see Fig. 5d). Values of convergence in these areas were between 1×10^{-4} and 2×10^{-4} s^{-1}. The northwesterly low-level flow below 5 km altitude at $D = 300$ and 3 km near $D = 500$ km transported particles toward the southeast end of the cross section and increased the particle concentration in that region (Fig. 5d). For $D < 450$ km, the particle concentration distribution exhibited numerous local maxima within a broad region of concentration between 500 and 800 particles per bin. These concentrations are less than the initial concentration value of 1000 particles per bin and can be attributed to divergent flow
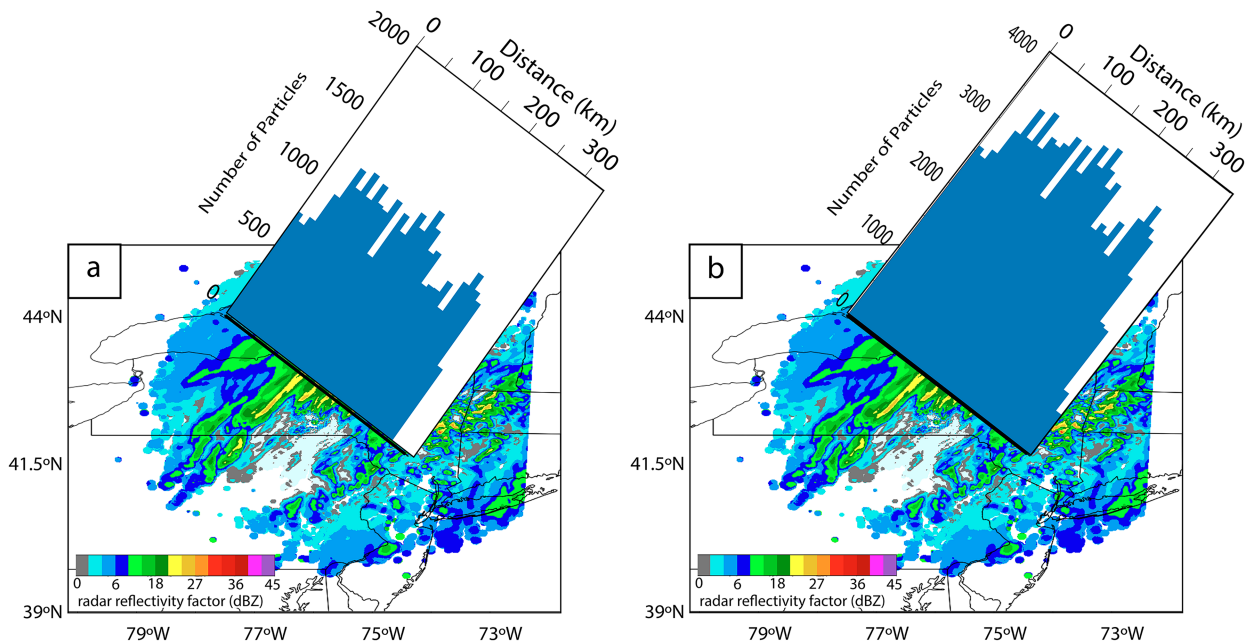
FIG. 12. As in Fig. 6, but for 1900 UTC 4 Feb 2022. (a) Overlay of 1-km-altitude particle concentration on top of radar reflectivity from KBGM, KTYX, and KENX at 1900 UTC 4 Feb 2022 for (a) particles released at 10 km and (b) particles released at 10, 8, and 6 km simultaneously.

below 4 km altitude at $D = 400$ km and below 2 km altitude at $D = 500$ km.

3) 4 FEBRUARY 2022 STORM

Figure 12a, the control experiment, shows the resulting particle concentration distribution at 1 km altitude overlaid on the KBGM, KTYX, and KENX WSR-88D reflectivity at 1900 UTC 4 February 2022. Here local maxima of particle concentration are collocated with very weak multibanded reflectivity structure located throughout central New York State. In particular, the radar composite near $D = 180$ km shows a weak multibanded region of reflectivity with values between 18 and 27 dBZ collocated directly with particle

distribution local maxima of 1100–1200 particles per bin. Toward the southeastern end of the cross section, near the Catskill Mountains of New York, several particle maxima are loosely collocated with increased reflectivity values although the reflectivity bands are slightly northeast of the axis of the cross section. Figure 12b, where particles were released from three altitudes, simultaneously shows similar results. Figures 13a–c, comparing particles released from three altitudes, shows only slightly greater reorganization of particles with greater residence time.

Figures 14a–i, with the same V_f, t_r, and z_i as Figs. 8a–i, display particle concentrations with many local minima and maxima in every panel. Unlike the other cases, the concentration
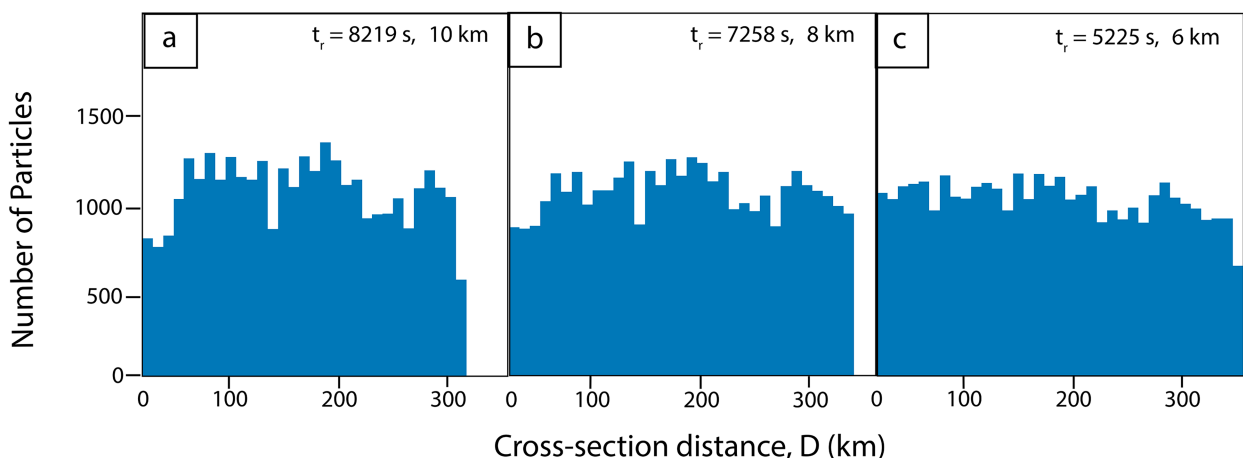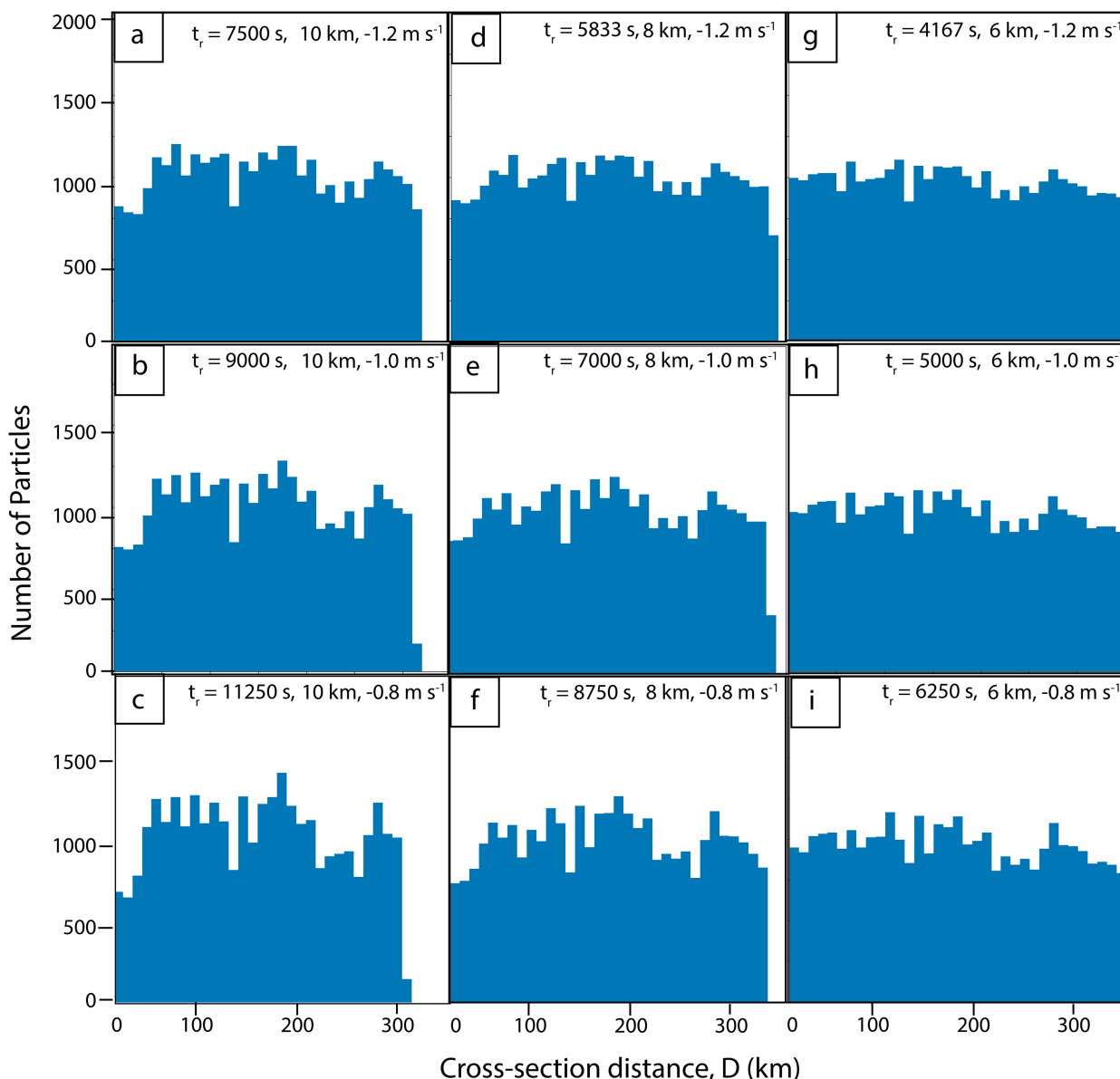

FIG. 13. As in Fig. 7, but for 4 Feb 2022.

FIG. 14. As in Fig. 8, but for 1900 UTC 4 Feb 2022.

distributions across all of the cross section deviated little from its original distribution owing to the weak v wind component and subsequent weak convergence along the cross section (see Fig. 5f). The weak convergent flow resulted in several local concentration maxima and minima that were relatively similar in magnitude, number, and location for all experiments.

4. Reorganization of particles by deformation

As the previous section illustrates, two-dimensional convergence normal to band orientation in the comma head of winter cyclones can increase particle concentrations in the vicinity of observed bands. A question remains as to whether deformation flow has the potential to further reorganize particles into linear features along the band axis. Whether deformation is sufficient to reorient particles into band-like features depends upon both the depth over which the deformation flow occurs, the magnitude of the deformation within the flow, and the residence time of the particles in the flow. In this section, we apply a simple model of deformation flow to quantify the magnitude of stretching of an initial field of ice particles falling at terminal velocity through deformation flow fields of various magnitudes and depths. The vertical profile of particle terminal velocity is parameterized as decreasing from -0.8 to -1.2 m s^{-1} in the same manner as the control experiments in the previous section using a 10 km cloud depth to account for microphysical particle growth. The kinematic framework uses a 500 km $\times$ 200 km $\times$ 10 km domain in x, y,
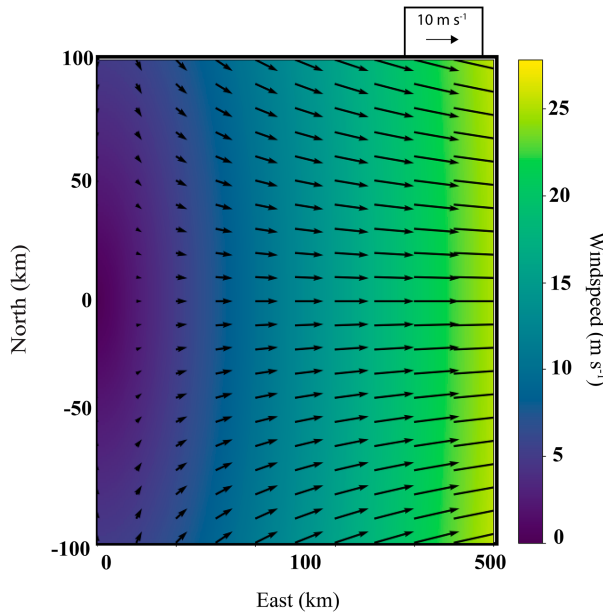
FIG. 15. Stretching deformation wind field (m s^{-1}) for $D = 1 \times 10^{-4}$ s^{-1} with the axis of dilatation at $y = 0$.

and z, respectively, with 1 km resolution, where x is the west–east direction, y is the north–south direction, and x is parallel to the axis of dilatation, which is along the x axis at $y = 0$, with z positive upward. Stretching deformation (D) is prescribed as constant with altitude within the deformation layer and is calculated as

$$D = \frac{\Delta u}{\Delta x} - \frac{\Delta v}{\Delta y}, \qquad (1)$$

where u and v are the wind components in the west–east and north–south directions, respectively. In the experiments which follow, five values of D ($D = 0.5 \times 10^{-4}$ s^{-1}, $D = 1 \times 10^{-4}$ s^{-1}, $D = 1.5 \times 10^{-4}$ s^{-1}, $D = 2 \times 10^{-4}$ s^{-1}, and $D = 2.5 \times 10^{-4}$ s^{-1}) were used, values chosen to be within the range reported within the comma heads of East Coast extratropical cyclones under conditions of frontogenesis (Novak et al. 2006). Figure 15 shows the deformation flow field with $D = 1 \times 10^{-4}$ s^{-1}. In the comma head of midlatitude winter cyclones, the deformation field typically transitions to quasi-linear jet streamflow in the vicinity of the frontal boundary, one to several kilometers in altitude above the surface (Fig. 16). Here, the jet streamflow above the deformation layer is assumed to be unidirectional and have no influence on particle reorganization. In the experiments that follow, the depth of the deformation layer in each experiment is varied from 1 to 10 km at 1 km intervals. Particles are assumed to fall through a 10 km depth, but particle reorganization only occurs within the deformation flow.

Figure 17a shows the initial particle arrangement just above the deformation layer. The particles were arranged at randomly placed points on the left side of the domain consistent with the arrangement described in Keeler et al. (2017) under conditions of no vertical wind shear at cloud top
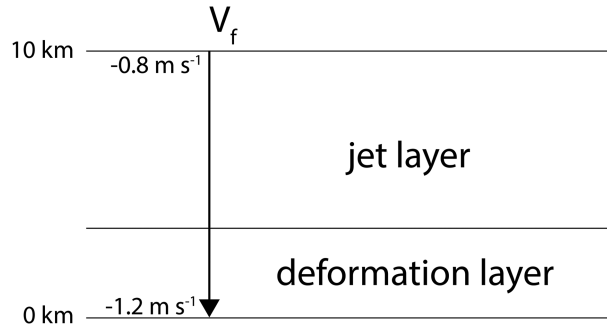
FIG. 16. Schematic of fall velocity profile and the jet and deformation layers used in the calculation.

(Fig. 17b). The remaining part of the domain allows sufficient space for particles to be transported eastward by the flow. Each red dot in Fig. 17a represents a circular cluster of particles emanating from a cloud-top generating cell with a 1 km radius. For this arrangement, L is the distance between the minimum and maximum location of ice particles along the x axis, while W is the distance between the minimum and the maximum location of ice particles on one side of the axis of dilatation along the y axis (Fig. 17a). The initial length to width ratio (LWR$_i$) at the top of the deformation layer was 0.5. The final length to width ratio at the surface (LWR$_s$) is shown in Fig. 18a. Any values greater than 0.5 represent stretching of the particle field along the axis of dilatation. The ratio R = LWR$_s$/LWR$_i$ provides a direct measure of the stretching of the initial ice particle field, and is shown in Fig. 18b.

As illustrated in Figs. 18a and 18b, the magnitude of stretching of the ice particle field depends upon the residence time of the particles within the deformation layer. As noted earlier, in the comma head of winter storms, deformation flow typically transitions to a quasi-linear flow in the vicinity of a frontal boundary that is commonly located around 1–4 km MSL (Rosenow et al. 2014; Varcie et al. 2023). The results shown in Figs. 18a and 18b for deformation depths at or below 4 km most likely represent a typical storm environment. In general, the stretching of the ice particle field is minimal when compared to stretching for much deeper (>7 km) deformation layers, especially with deformation greater than 1×10^{-4} s^{-1}. For example, with a deformation layer depth of 4 km, only with the two strongest deformation fields at 2×10^{-4} and 2.5×10^{-4} s^{-1} was there a doubling of the length of the particle field along the axis of dilatation with LWR$_s$ values of 1.04 and 1.24 and R values of 2.08 and 2.48, respectively. For deformation layers shallower than 4 km, the stretching of the surface ice particle field was less than double that of the original field for all deformation magnitudes. These results indicate that in the comma-head region of winter cyclones, layers of deformation flow having a depth of 4 km or less are likely to produce minimal particle reorganization along the axis of dilatation.

5. Conclusions

In this paper we conducted two separate experiments to explore how flow kinematics can reorganize snowfall beneath
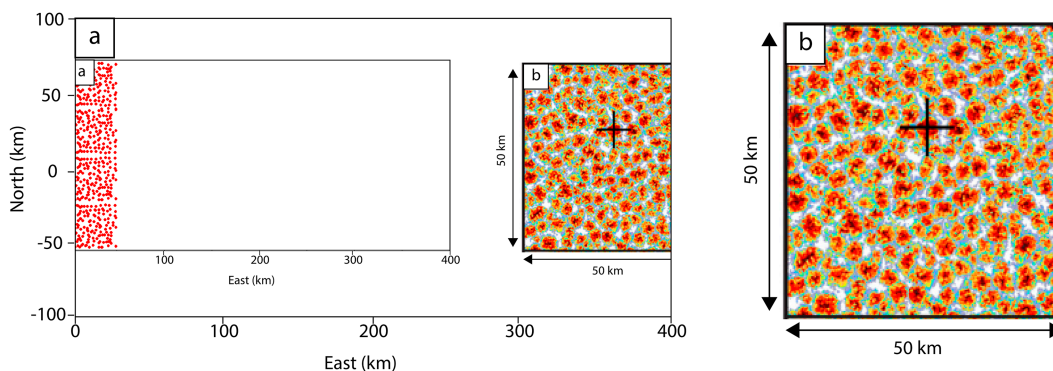
FIG. 17. (a) Initial ice particle field arrangement based upon (b) from Keeler et al. (2017).

cloud-top generating cells. The first experiment explored whether particles falling beneath cloud top from uniformly spaced generating cells at terminal velocity within observed 2D convergent wind fields can be reorganized consistent with the presence of single and multibanded structures present on WSR-88D radars. This experiment demonstrated that the greater the residence time in each of the three storms, the greater the particle reorganization by the two-dimensional flow field beneath cloud top, resulting in larger concentrations of particles in the vicinity of observed precipitation bands. The second experiment examined the role of flow deformation in the reorganization of ice particles placed randomly at cloud top using an idealized kinematic model with particle fall velocities and stretching deformation flow having magnitudes and depths characteristic of winter cyclones. This study found the deformation alone is likely insufficient to reorganize falling particles in typical winter storm environments.

As noted in the introduction, banded precipitation observed on surveillance radars within the comma head of winter cyclones can occur as a result of any or all of the following three factors: 1) kinematic flow rearranging snowfall beneath cloud top into linear banded features near the surface, 2) snow growth as a

result of large-scale ascent in an elongated updraft in the secondary circulation associated with frontogenesis, or 3) snow growth due to ascent in convection from the release of mesoscale instabilities within the updraft associated with frontogenesis. The first experiment investigated the first factor by elucidating the role of two-dimensional convergence in reorganizing snowfall beneath cloud top. Results from the first experiment show that the two-dimensional convergent flow in each case resulted in an increase of particle concentrations that were in the vicinity of the low-level observed precipitation bands on radar. The experiments with maximum residence time, having both varying and constant particle fall velocities, especially in the first two storms, exhibited the greatest particle concentrations near the bands as particles were subject to convergent flow regions for a longer duration. This suggests that for a large particle fall depth, fall velocities becoming more negative with decreasing altitude and regions of convergent flow, kinematics alone can assist in band formation by locally increasing particle concentrations. While the findings give information on the concentration of particles into band regions within the comma head, they do not definitively determine the cause of precipitation banding, since the
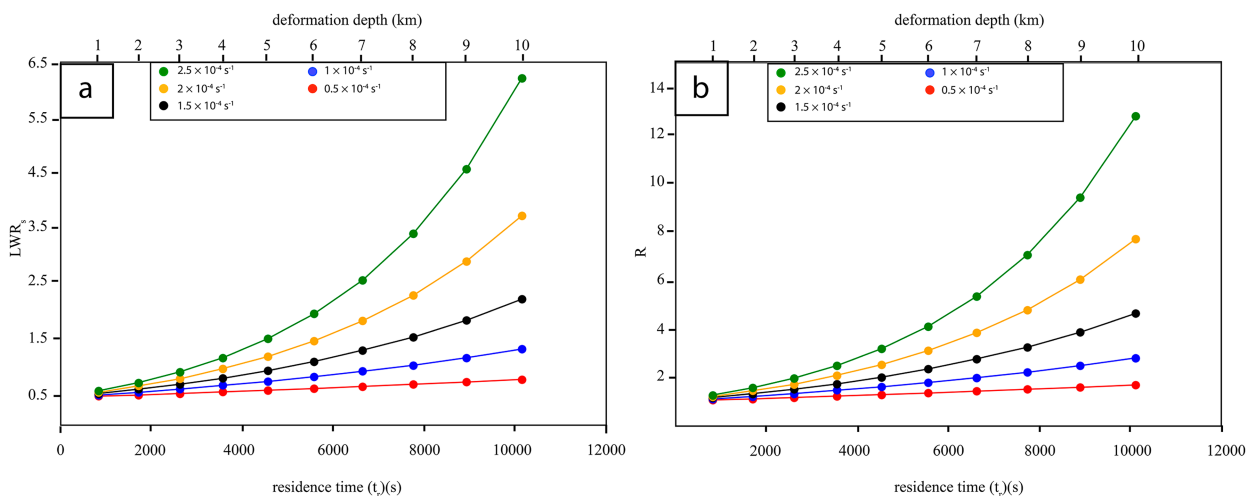

FIG. 18. (a) LWR_s and (b) R for all deformation layer depths and magnitudes. The residence time (s) of particles in the deformation layer is also shown.

latter two factors were not considered. We note that these findings are limited to the comma-head region and may not apply to banded features in other parts of extratropical cyclones.

The second experiment, testing the role of deformation flow on particle reorganization given typical deformation layer depths and magnitudes in midlatitude winter storms showed that deformation provides for little particle reorganization given typical deformation layer depths and magnitudes within the comma head of such storms. This suggests that the primary cause of particle reorganization by kinematics is through convergent flow across frontal zones within winter cyclone flow structure, while deformation flow contributes marginally to particle reorganization in winter storm environments.

Data availability statement. Profiling of Winter Storms (PLOWs) W-band Wyoming Cloud Radar data used to construct Fig. 6 are available at https://data.eol.ucar.edu/master_lists/generated/plows/. IMPACTS lidar and W-band CRS data used to construct Figs. 5 and 7 are available from the NASA EOSDIS Global Hydrology Resource Center Distributed Active Archive Center, Huntsville, Alabama, DOI: https://doi.org/10.5067/IMPACTS/DATA101.

REFERENCES

American Meteorological Society, 2023: Generating cell. Glossary of Meteorology, http://glossary.ametsoc.org/wiki/generating_cell.

Bergeron, T., 1928: Über die dreidimensional verknüpfende wetteranalyse. *Geophys. Publ.*, **5**, 1–111.

——, 1950: Über der mechanismum der ausgeibigen Niederschläge. *Ber. Dtsch. Wetterdienstes*, **12**, 225–232.

Browning, K. A., 1983: Air motion and precipitation growth in a major snowstorm. *Quart. J. Roy. Meteor. Soc.*, **109**, 225–242, https://doi.org/10.1002/qj.49710945911.

Carbone, R. E., and A. R. Bohne, 1975: Cellular snow generation—A Doppler radar study. *J. Atmos. Sci.*, **32**, 1384–1394, https://doi.org/10.1175/1520-0469(1975)032<1384:CSGDRS>2.0.CO;2.

Cunningham, J. G., and S. E. Yuter, 2014: Instability characteristics of radar-derived mesoscale organization modes within cool-season precipitation near Portland, Oregon. *Mon. Wea. Rev.*, **142**, 1738–1757, https://doi.org/10.1175/MWR-D-13-00133.1.

Douglas, R. H., K. L. S. Gunn, and J. S. Marshall, 1957: Pattern in the vertical of snow generation. *J. Meteor.*, **14**, 95–114, https://doi.org/10.1175/1520-0469(1957)014<0095:PITVOS>2.0.CO;2.

Draxler, R. R., and G. D. Hess, 1998: An overview of the HYSPLIT_4 modelling system for trajectories, dispersion, and deposition. *Aust. Meteor. Mag.*, **47**, 295–308.

Emanuel, K. A., 1985: Frontal circulations in the presence of small moist symmetric stability. *J. Atmos. Sci.*, **42**, 1062–1071, https://doi.org/10.1175/1520-0469(1985)042%3C1062:FCITPO%3E2.0.CO;2.

EOL/PLOWs, 2023: Wyoming Cloud Radar data. Accessed 6 January 2023, https://data.eol.ucar.edu/master_lists/generated/plows/.

Ganetis, S. A., B. A. Colle, S. E. Yuter, and N. P. Hoban, 2018: Environmental conditions associated with observed snowband structures within northeast U.S. winter storms. *Mon. Wea. Rev.*, **146**, 3675–3690, https://doi.org/10.1175/MWR-D-18-0054.1.

Gunn, K. L. S., M. P. Langleben, A. S. Dennis, and B. A. Power, 1954: Radar evidence of a generating level for snow. *J. Meteor.*, **11**, 20–26, https://doi.org/10.1175/1520-0469(1954)011<0020:REOAGL>2.0.CO;2.

Herzegh, P. H., and P. V. Hobbs, 1980: The mesoscale and microscale structure and organization of clouds and precipitation in midlatitude cyclones. II: Warm-frontal clouds. *J. Atmos. Sci.*, **37**, 597–611, https://doi.org/10.1175/1520-0469(1980)037<0597:TMAMSA>2.0.CO;2.

Heymsfield, A., 1972: Ice crystal terminal velocities. *J. Atmos. Sci.*, **29**, 1348–1357, https://doi.org/10.1175/1520-0469(1972)029<1348:ICTV>2.0.CO;2.

Hobbs, P. V., and J. D. Locatelli, 1978: Rainbands, precipitation cores, and generating cells in a cyclonic storm. *J. Atmos. Sci.*, **35**, 230–241, https://doi.org/10.1175/1520-0469(1978)035<0230:RPCAGC>2.0.CO;2.

Houze, R. A., Jr., S. A. Rutledge, T. J. Matejka, and P. V. Hobbs, 1981: The mesoscale and microscale structure and organization of clouds and precipitation in midlatitude cyclones. III: Air motions and precipitation growth in a warm-frontal rainband. *J. Atmos. Sci.*, **38**, 639–649, https://doi.org/10.1175/1520-0469(1981)038<0639:TMAMSA>2.0.CO;2.

Keeler, J. M., B. F. Jewett, R. M. Rauber, G. M. McFarquhar, R. M. Rasmussen, L. Xue, C. Liu, and G. Thompson, 2016a: Dynamics of cloud-top generating cells in winter cyclones. Part I: Idealized simulations in the context of field observations. *J. Atmos. Sci.*, **73**, 1507–1527, https://doi.org/10.1175/JAS-D-15-0126.1.

——, ——, ——, ——, ——, ——, ——, and ——, 2016b: Dynamics of cloud-top generating cells in winter cyclones. Part II: Radiative and instability forcing. *J. Atmos. Sci.*, **73**, 1529–1553, https://doi.org/10.1175/JAS-D-15-0127.1.

——, ——, ——, ——, ——, ——, ——, and ——, 2017: Dynamics of cloud-top generating cells in winter cyclones. Part III: Shear and convective organization. *J. Atmos. Sci.*, **74**, 2879–2897, https://doi.org/10.1175/JAS-D-16-0314.1.

Kumjian, M. R., and K. A. Lombardo, 2017: Insights into the evolving microphysical and kinematic structure of northeastern U.S. winter storms from dual-polarization Doppler radar. *Mon. Wea. Rev.*, **145**, 1033–1061, https://doi.org/10.1175/MWR-D-15-0451.1.

——, S. A. Rutledge, R. M. Rasmussen, P. C. Kennedy, and M. Dixon, 2014: High-resolution polarimetric radar observations of snow-generating cells. *J. Appl. Meteor. Climatol.*, **53**, 1636–1658, https://doi.org/10.1175/JAMC-D-13-0312.1.

Lackmann, G. M., and G. Thompson, 2019: Hydrometeor lofting and mesoscale snowbands. *Mon. Wea. Rev.*, **147**, 3879–3899, https://doi.org/10.1175/MWR-D-19-0036.1.

Marshall, J. S., 1953: Precipitation trajectories and patterns. *J. Meteor.*, **10**, 25–29, https://doi.org/10.1175/1520-0469(1953)010%3C0025:PTAP%3E2.0.CO;2.

Matejka, T. J., R. A. Houze Jr., and P. V. Hobbs, 1980: Microphysics and dynamics of clouds associated with mesoscale rainbands in extratropical cyclones. *Quart. J. Roy. Meteor. Soc.*, **106**, 29–56, https://doi.org/10.1002/qj.49710644704.

McFarquhar, G. M., and Coauthors, 2011: Indirect and Semi-Direct Aerosol Campaign (ISDAC): The impact of Arctic aerosols on

clouds. *Bull. Amer. Meteor. Soc.*, **92**, 183–201, https://doi.org/10.1175/2010BAMS2935.1.

McGill, M., D. Hlavka, W. Hart, V. S. Scott, J. Spinhirne, and B. Schmid, 2002: Cloud Physics Lidar: Instrument description and initial measurement results. *Appl. Opt.*, **41**, 3725–3734, https://doi.org/10.1364/AO.41.003725.

McMurdie, L. A., G. Heymsfield, J. E. Yorks, and S. A. Braun, 2019: Investigation of Microphysics and Precipitation for Atlantic Coast-Threatening Snowstorms (IMPACTS) collection. NASA EOSDIS Global Hydrology Resource Center Distributed Active Archive Center, accessed 6 January 2023, https://doi.org/10.5067/IMPACTS/DATA101.

——, and Coauthors, 2022: Chasing snowstorms: The Investigation of Microphysics and Precipitation for Atlantic Coast-Threatening Snowstorms (IMPACTS) campaign. *Bull. Amer. Meteor. Soc.*, **103**, E1243–E1269, https://doi.org/10.1175/BAMS-D-20-0246.1.

Mitchell, D. L., 1996: Use of mass- and area-dimensional power laws for determining precipitation particle terminal velocities. *J. Atmos. Sci.*, **53**, 1710–1723, https://doi.org/10.1175/1520-0469(1996)053<1710:UOMAAD>2.0.CO;2.

Nicosia, D. J., and R. H. Grumm, 1999: Mesoscale band formation in three major northeastern United States snowstorms. *Wea. Forecasting*, **14**, 346–368, https://doi.org/10.1175/1520-0434(1999)014<0346:MBFITM>2.0.CO;2.

Novak, D. R., L. F. Bosart, D. Keyser, and J. S. Waldstreicher, 2004: An observational study of cold season–banded precipitation in northeast U.S. cyclones. *Wea. Forecasting*, **19**, 993–1010, https://doi.org/10.1175/815.1.

——, J. S. Waldstreicher, D. Keyser, and L. F. Bosart, 2006: A forecast strategy for anticipating cold season mesoscale band formation within eastern U.S. cyclones. *Wea. Forecasting*, **21**, 3–23, https://doi.org/10.1175/WAF907.1.

——, B. A. Colle, and S. E. Yuter, 2008: High-resolution observations and model simulations of the life cycle of an intense mesoscale snowband over the northeastern United States. *Mon. Wea. Rev.*, **136**, 1433–1456, https://doi.org/10.1175/2007MWR2233.1.

——, ——, and R. McTaggart-Cowan, 2009: The role of moist processes in the formation and evolution of mesoscale snowbands within the comma head of northeast U.S. cyclones. *Mon. Wea. Rev.*, **137**, 2662–2686, https://doi.org/10.1175/2009MWR2874.1.

——, ——, and A. R. Aiyyer, 2010: Evolution of mesoscale precipitation band environments within the comma head of northeast U.S. cyclones. *Mon. Wea. Rev.*, **138**, 2354–2374, https://doi.org/10.1175/2010MWR3219.1.

Petterssen, S., 1936: Contribution to the theory of frontogenesis. *Geofys. Publ.*, **11**, 1–27.

Plummer, D. M., G. M. McFarquhar, R. M. Rauber, B. F. Jewett, and D. C. Leon, 2014: Structure and statistical analysis of the microphysical properties of generating cells in the comma head region of continental winter cyclones. *J. Atmos. Sci.*, **71**, 4181–4203, https://doi.org/10.1175/JAS-D-14-0100.1.

——, ——, ——, ——, and ——, 2015: Microphysical properties of convectively generated fall streaks within the stratiform comma head region of continental winter cyclones. *J. Atmos. Sci.*, **72**, 2465–2483, https://doi.org/10.1175/JAS-D-14-0354.1.

Pruppacher, H. R., and J. D. Klett, 1997: *Microphysics of Clouds and Precipitation*. 2nd ed. Kluwer Academic, 954 pp.

Rauber, R. M., and Coauthors, 2014a: Stability and charging characteristics of the comma head region of continental winter

cyclones. *J. Atmos. Sci.*, **71**, 1559–1582, https://doi.org/10.1175/JAS-D-13-0253.1.

——, M. K. Macomber, D. M. Plummer, A. A. Rosenow, G. M. McFarquhar, B. F. Jewett, D. Leon, and J. M. Keeler, 2014b: Finescale radar and airmass structure of the comma head of a continental winter cyclone: The role of three airstreams. *Mon. Wea. Rev.*, **142**, 4207–4229, https://doi.org/10.1175/MWR-D-14-00057.1.

——, S. M. Ellis, J. Vivekanandan, J. Stith, W.-C. Lee, G. M. McFarquahar, B. F. Jewett, and A. Janiszeski, 2017: Finescale structure of a snowstorm over the northeastern United States: A first look at high-resolution HIAPER cloud radar observations. *Bull. Amer. Meteor. Soc.*, **98**, 253–269, https://doi.org/10.1175/BAMS-D-15-00180.1.

Rosenow, A. A., D. M. Plummer, R. M. Rauber, G. M. McFarquhar, B. F. Jewett, and D. Leon, 2014: Vertical velocity and physical structure of generating cells and convection in the comma head region of continental winter cyclones. *J. Atmos. Sci.*, **71**, 1538–1558, https://doi.org/10.1175/JAS-D-13-0249.1.

Rutledge, S. A., and P. Hobbs, 1983: The mesoscale and microscale structure and organization of clouds and precipitation in midlatitude cyclones. VIII: A model for the "seeder-feeder" process in warm-frontal rainbands. *J. Atmos. Sci.*, **40**, 1185–1206, https://doi.org/10.1175/1520-0469(1983)040<1185:TMAMSA>2.0.CO;2.

Sanders, F., 1955: An investigation of the structure and dynamics of an intense surface frontal zone. *J. Meteor.*, **12**, 542–552, https://doi.org/10.1175/1520-0469(1955)012<0542:AIOTSA>2.0.CO;2.

——, 1986: Frontogenesis and symmetric stability in a major New England snowstorm. *Mon. Wea. Rev.*, **114**, 1847–1862, https://doi.org/10.1175/1520-0493(1986)114<1847:FASSIA>2.0.CO;2.

——, and L. F. Bosart, 1985: Mesoscale structure in the megalopolitan snowstorm of 11–12 February 1983. Part I: Frontogenetical forcing and symmetric instability. *J. Atmos. Sci.*, **42**, 1050–1061, https://doi.org/10.1175/1520-0469(1985)042<1050:MSITMS>2.0.CO;2.

Schultz, D. M., and P. N. Schumacher, 1999: The use and misuse of conditional symmetric instability. *Mon. Wea. Rev.*, **127**, 2709–2732, https://doi.org/10.1175/1520-0493(1999)127%3C2709:TUAMOC%3E2.0.CO;2; Corrigendum, **128**, 1573, https://doi.org/10.1175/1520-0493(1999)127<1573:CORRIG>2.0.CO;2.

——, and J. A. Knox, 2007: Banded convection caused by frontogenesis in a conditionally, symmetrically, and inertially unstable environment. *Mon. Wea. Rev.*, **135**, 2095–2110, https://doi.org/10.1175/MWR3400.1.

——, D. S. Arndt, D. J. Stensrud, and J. W. Hanna, 2004: Snowbands during the cold-air outbreak of 23 January 2003. *Mon. Wea. Rev.*, **132**, 827–842, https://doi.org/10.1175/1520-0493(2004)132<0827:SDTCOO>2.0.CO;2.

Sienkiewicz, J. M., J. D. Locatelli, P. V. Hobbs, and B. Geerts, 1989: Organization and structure of clouds and precipitation on the mid-Atlantic coast of the United States. Part II: The mesoscale and microscale structures of some frontal rainbands. *J. Atmos. Sci.*, **46**, 1349–1364, https://doi.org/10.1175/1520-0469(1989)046<1349:OASOCA>2.0.CO;2.

Stark, D., B. A. Colle, and S. E. Yuter, 2013: Observed microphysical evolution for two East Coast winter storms and the associated snow bands. *Mon. Wea. Rev.*, **141**, 2037–2057, https://doi.org/10.1175/MWR-D-12-00276.1.

Stone, P. H., 1966: Frontogenesis by horizontal wind deformation fields. *J. Atmos. Sci.*, **23**, 455–465, https://doi.org/10.1175/1520-0469(1966)023<0455:FBHWDF>2.0.CO;2.

Syrett, W. J., B. A. Albrecht, and E. E. Clothiaux, 1995: Vertical cloud structure in a midlatitude cyclone from a 94-GHz radar. *Mon. Wea. Rev.*, **123**, 3393–3407, https://doi.org/10.1175/1520-0493(1995)123<3393:VCSIAM>2.0.CO;2.

Thorpe, A. J., and K. A. Emanuel, 1985: Frontogenesis in the presence of small stability to slantwise convection. *J. Atmos. Sci.*, **42**, 1809–1824, https://doi.org/10.1175/1520-0469(1985)042<1809:FITPOS>2.0.CO;2.

Varcie, M. M., and Coauthors, 2023: Precipitation growth processes in the comma-head region of the 7 February 2020 northeast snowstorm: Results from IMPACTS. *J. Atmos. Sci.*, **80**, 3–29, https://doi.org/10.1175/JAS-D-22-0118.1.

Walker McLinden, M. L., L. Li, G. M. Heymsfield, M. Coon, and A. Emory, 2021: The NASA GSFC 94-GHz airborne solid-state Cloud Radar System (CRS). *J. Atmos. Oceanic Technol.*, **38**, 1001–1017, https://doi.org/10.1175/JTECH-D-20-0127.1.

Wexler, R., 1955: Radar analysis of precipitation streamers observed 25 February 1954. *J. Meteor.*, **12**, 391–393, https://doi.org/10.1175/1520-0469(1955)012<0391:RAOPSO>2.0.CO;2.

——, and D. Atlas, 1959: Precipitation generating cells. *J. Meteor.*, **16**, 327–332, https://doi.org/10.1175/1520-0469(1959)016<0327:PGC>2.0.CO;2.

Yang, M., R. M. Rauber, and M. K. Ramamurthy, 2001: Origin, evolution, and finescale structure of the St. Valentine's Day mesoscale gravity wave observed during STORM-FEST. Part II: Finescale structure. *Mon. Wea. Rev.*, **129**, 218–236, https://doi.org/10.1175/1520-0493(2001)129<0218:OEAFSO>2.0.CO;2.

Yorks, J. E., D. L. Hlavka, M. A. Vaughan, M. J. McGill, W. D. Hart, S. Rodier, and R. Kuehn, 2011: Airborne validation of cirrus cloud properties derived from CALIPSO lidar measurements: Spatial properties. *J. Geophys. Res.*, **116**, D19207, https://doi.org/10.1029/2011JD015942.